Finite-difference time-domain calculation of spontaneous emission lifetime in a microcavity

Y. Xu, J. S. Vučković, R. K. Lee, O. J. Painter, A. Scherer, and A. Yariv

Departments of Applied Physics and Electrical Engineering, California Institute of Technology, MS 128-95, Pasadena, California 91125

Received October 30, 1998

We developed a general numerical method to calculate the spontaneous emission lifetime in an arbitrary microcavity, using a finite-difference time-domain algorithm. For structures with rotational symmetry we also developed a more efficient but less general algorithm. To simulate an open radiation problem, we use absorbing boundaries to truncate the computational domain. The accuracy of this method is limited only by numerical error and finite reflection at the absorbing boundaries. We compare our result with cases that can be solved analytically and find excellent agreement. Finally, we apply the method to calculate the spontaneous emission lifetime in a slab waveguide and in a dielectric microdisk, respectively. © 1999 Optical Society of America [S0740-3224(99)00403-8]

OCIS codes: 000.4430, 230.3990, 270.5580.

1. INTRODUCTION

The possibility of changing the spontaneous emission lifetime with cavity structures was first proposed by Purcell.[1] Owing to the practical importance of controlling electron–photon interaction in microcavities, a great deal of recent theoretical and experimental work has been devoted to this topic.[2] Many microcavities proposed in the literature, such as the VCSEL's and microdisk lasers, have relatively simple geometries such that the spontaneous emission lifetime can be calculated analytically with some simplifying approximations. With the advent of photonic crystals[3,4] it is possible to form a photonic bandgap and control light emission in all directions. However, the analytical calculation of spontaneous emission properties in photonic crystals is much more difficult, owing to the complex geometries of two-dimensional (2D) and three-dimensional (3D) photonic crystals.

In principle, one should calculate spontaneous emission lifetime with quantum electrodynamics. However, it can be shown that classical electrodynamics gives results identical to those of quantum mechanics.[5] In a classical picture the dipole radiation field acts on the oscillating dipole and causes the dipole moment to decay, which accounts for the spontaneous emission. Since the classical approach can be implemented more easily numerically, in this paper we use classical electrodynamics to calculate spontaneous emission lifetime.

It was Yee[6] who first used the finite-difference time-domain (FDTD) algorithm to numerically solve Maxwell's equations. Since then FDTD has been extensively used in electromagnetic computations. With this method a space mesh is introduced and Maxwell's equations are transformed into a set of finite-difference equations on that space mesh. By numerically solving the finite-difference equations, we can obtain the electromagnetic radiation field of an oscillating dipole in a microcavity, from which the spontaneous emission lifetime can be derived. Since this is an open radiation problem, an absorbing boundary condition is needed to truncate the FDTD computational domain. We employ the perfectly matched layer[7] (PML) proposed recently by Berenger.

We also developed an algorithm to calculate spontaneous emission lifetime in structures with rotational symmetry, which is a generalization of Chen's method.[8] With the rotational symmetry, this algorithm effectively reduces the original 3D problem to a 2D problem, thus resulting in significant savings in computational memory and time. Since in the past few years many experimentally fabricated microcavities, such as microdisk lasers and VCSEL's, are rotationally symmetric, this method is of practical importance.

This paper is organized as follows. In Section 2 we use classical electrodynamics to calculate the radiation power of a dipole in a microcavity and show that the spontaneous emission lifetime can be derived from the dipole radiation power. In Section 3 we explain our numerical algorithms in detail. Then in Section 4 we test them in three cases. First, we calculate the spontaneous emission rate in a waveguide formed by two parallel perfect-metal plates. Comparing our result with the analytical result in Ref. 5, we find excellent agreement. In the next example we calculate the spontaneous emission rate in a slab waveguide as a function of the waveguide thickness. To show the usefulness of our algorithm, in the third case we compute the spontaneous emission rate in a dielectric microdisk. Finally, we summarize in Section 5.

2. CLASSICAL ANALYSIS OF SPONTANEOUS EMISSION

It is well known that the phenomenon of spontaneous emission can be accounted for classically.[9] The sponta-

neous emission rate can be understood as the rate of transfer of energy from the radiating dipole to the electromagnetic field. In this section we follow the approach in Ref. 5, expand the dipole radiation field in a complete set of orthonormal modes, and express the dipole radiation power in terms of those orthonormal modes.

The electric field of an oscillating dipole in a cavity can be separated into a longitudinal part and a transverse part.[10] The longitudinal electric field is the unretarded Coulomb field that is due to the dipole source and the cavity surrounding it, which does not contribute to the dipole radiation power and is neglected in this paper (for definitions of the transverse field and the longitudinal field and for the proof of this statement, see Appendix A). The transverse electric field of an oscillating dipole must satisfy[11]

$$\nabla \cdot [\epsilon(\mathbf{x})\mathbf{E}(\mathbf{x}, t)] = 0, \quad (1)$$

$$\nabla \times [\nabla \times \mathbf{E}(\mathbf{x}, t)] + \epsilon(\mathbf{x})\mu_0 \frac{\partial^2 \mathbf{E}(\mathbf{x}, t)}{\partial t^2} + \mu_0 \frac{\partial^2 \mathbf{P}(\mathbf{x}, t)}{\partial t^2} + \mu_0 \frac{\partial \mathbf{J}(\mathbf{x}, t)}{\partial t} = 0, \quad (2)$$

where the $\epsilon(\mathbf{x})$ is the dielectric constant of the microcavity. In this paper we limit ourselves to the case of linear lossless dielectric media and assume $\epsilon(\mathbf{x})$ to be a real number. However, our analysis can be easily generalized to take the medium loss or amplification into account.

The dipole source in the above equation is represented by $\mathbf{P}(\mathbf{x}, t)$:

$$\mathbf{P}(\mathbf{x}, t) = d(t)\hat{d}\,\delta(\mathbf{x} - \mathbf{x}_0), \quad (3)$$

where $d(t)$ and $\hat{d}$ are the magnitude and the polarization, respectively, of the oscillating dipole. This dipole is assumed to be a point source located at position $\mathbf{x}_0$ and thus has the distribution of a δ function. For convenience of analysis we also introduce a dissipation current $\mathbf{J}(\mathbf{x}, t)$, which is assumed to be a linear function of the electric field

$$\mathbf{J}(\mathbf{x}, t) = \gamma\epsilon(\mathbf{x})\mathbf{E}(\mathbf{x}, t). \quad (4)$$

The magnitude of the proportionality constant γ is of no real consequence, since we let it go to zero at the end of calculation in the case of a lossless cavity.

We expand the radiation electric field in terms of a complete set of transverse modes $\{\mathbf{F}_n(\mathbf{x})\}$, which is defined in Ref. 11:

$$\mathbf{E}(\mathbf{x}, t) = \sum_n \alpha_n(t)\mathbf{F}_n(\mathbf{x}). \quad (5)$$

These modes $\{\mathbf{F}_n(\mathbf{x})\}$ obey the following eigenmode equation[11]:

$$\nabla \times [\nabla \times \mathbf{F}_n(\mathbf{x})] = \epsilon(\mathbf{x})\mu_0\omega_n^2\mathbf{F}_n(\mathbf{x}), \quad (6)$$

where ω_n is the frequency of the nth mode and they are also orthonormal to each other[11]:

$$\int \mathrm{d}^3x\,\epsilon(\mathbf{x})\mathbf{F}_n^*(\mathbf{x}) \cdot \mathbf{F}_m(\mathbf{x}) = \delta_{m,n}. \quad (7)$$

Substituting Eqs. (3)–(5) into Eq. (2), we have

$$\mu_0\epsilon(\mathbf{x})\sum_n \{\ddot{\alpha}_n(t) + \gamma\dot{\alpha}_n(t)\}\mathbf{F}_n(\mathbf{x}) + \sum_n \alpha_n(t)\nabla \times [\nabla \times \mathbf{F}_n(\mathbf{x})] = -\mu_0\ddot{d}(t)\hat{d}\,\delta(\mathbf{x} - \mathbf{x}_0), \quad (8)$$

and then using Eqs. (6) and (7), we find the equation of motion for the mode amplitude $\alpha_n(t)$:

$$\ddot{\alpha}_n(t) + \gamma\dot{\alpha}_n(t) + \omega_n^2\alpha_n(t) = -\ddot{d}(t)[\hat{d} \cdot \mathbf{F}_n^*(\mathbf{x}_0)]. \quad (9)$$

Assume the dipole oscillates at a single frequency ω_0 and a constant amplitude μ:

$$d(t) = \mu \exp(-i\omega_0 t). \quad (10)$$

When we solve Eq. (9), the mode amplitude $\alpha_n(t)$ for the nth mode $\mathbf{F}_n(\mathbf{x})$ is

$$\alpha_n(t) = d(t)\frac{\omega_0^2}{\omega_n^2 - \omega_0^2 - i\omega_0\gamma}[\hat{d} \cdot \mathbf{F}_n^*(\mathbf{x}_0)]. \quad (11)$$

The dipole emission power is given by the integral[10]

$$P_{\text{classical}} = -\frac{1}{2}\mathrm{Re}\left[\int \mathrm{d}^3x \frac{\partial \mathbf{P}^*(\mathbf{x}, t)}{\partial t} \cdot \mathbf{E}(\mathbf{x}, t)\right]. \quad (12)$$

When we substitute Eq. (5) and Eq. (11) into the above equation, the result for the classical spontaneous emission power is

$$P_{\text{classical}} = \frac{1}{4}\omega_0^2\mu^2\sum_n |\hat{d} \cdot \mathbf{F}_n(\mathbf{x}_0)|^2 \frac{\gamma/2}{(\omega_n - \omega_0)^2 + \gamma^2/4}. \quad (13)$$

Since we are dealing with lossless material, let $\gamma \to 0$ such that the Lorentzian becomes a delta function:

$$\lim_{\gamma \to 0} \frac{\gamma/2}{(\omega_n - \omega_0)^2 + \gamma^2/4} = \pi\delta(\omega_n - \omega_0). \quad (14)$$

Finally, the classical radiation power is given by

$$P_{\text{classical}} = \frac{1}{4}\pi\mu^2\omega_0^2\sum_n |\hat{d} \cdot \mathbf{F}_n(\mathbf{x}_0)|^2\delta(\omega_n - \omega_0). \quad (15)$$

Compare the above result with that for the spontaneous emission power derived from cavity quantum electrodynamics considerations[5,11]:

$$P_{\text{quantum}} = \frac{\hbar\omega_{\text{eg}}}{\tau_{\text{spon}}} = \pi\omega_{\text{eg}}^2\mu_{\text{eg}}^2\sum_n |\hat{d} \cdot \mathbf{F}_n(\mathbf{x}_0)|^2\delta(\omega_n - \omega_{\text{eg}}), \quad (16)$$

where ω_{eg} is the transition frequency from the excited state to the ground state, μ_{eg} is the dipole matrix element between the excited state and the ground state, and τ_{spon} is the spontaneous emission lifetime given by Fermi's golden rule. If we identify μ and ω_0 in Eq. (15) with μ_{eg} and ω_{eg}, respectively, in Eq. (16), the two expressions differ only by a factor of 4. This proportionality allows us to calculate the spontaneous emission rate with the classical dipole radiation power $P_{\text{classical}}$. For the spontaneous

emission lifetime $\tau_{\text{spon}}^{\text{bulk}}$ in bulk material and the spontaneous emission lifetime $\tau_{\text{spon}}^{\text{cavity}}$ in a microcavity, after dividing Eq. (16) by Eq. (15), we have the following relation:

$$\frac{\tau_{\text{spon}}^{\text{bulk}}}{\tau_{\text{spon}}^{\text{cavity}}} = \frac{P_{\text{classical}}^{\text{cavity}}}{P_{\text{classical}}^{\text{bulk}}}, \tag{17}$$

where $P_{\text{classical}}^{\text{cavity}}$ is the classical radiation power for a dipole in a microcavity and $P_{\text{classical}}^{\text{bulk}}$ is the dipole emission power in a bulk dielectric material.

Thus to calculate the change of the spontaneous emission rate in a microcavity, we can first classically calculate the radiation field of a dipole in the microcavity then integrate the Poynting vector of that radiation field over a surface that encloses the dipole source. The integration gives us the dipole radiation power, from which the modification of spontaneous emission lifetime can be extracted.

3. NUMERICAL ALGORITHMS

A. Finite-Difference Time-Domain Algorithm for the Three-Dimensional Geometries

A FDTD method[6] is used in this algorithm to calculate the dipole radiation field. We start from two of Maxwell's equations:

$$\mu_0 \frac{\partial \mathbf{H}}{\partial t} = -\nabla \times \mathbf{E}, \tag{18a}$$

$$\epsilon \frac{\partial \mathbf{E}}{\partial t} = \nabla \times \mathbf{H} - \frac{\partial \mathbf{P}}{\partial t}. \tag{18b}$$

It should be mentioned that, even though we only use two of Maxwell's equations, the numerical solutions satisfy all four Maxwell's equations (see Appendix B for proof). To discretize the above equations, following Yee,[6] we introduce a space grid and denote the grid point as

$$(i, j, k) = (i\Delta x, j\Delta y, k\Delta z) \tag{19}$$

and any function of space and time as

$$F^n(i, j, k) = F(i\Delta x, j\Delta y, k\Delta z, n\Delta t), \tag{20}$$

where Δx, Δy, and Δz are the space increments in the x, y, and z directions and Δt is the time increment. Placing the electromagnetic field and the dipole moment on the space grid as in Fig. 1, evolving the **E** and the **H** fields in the time domain at alternate half-time steps, and applying the finite-difference approximation, we can find a set of finite-difference equations for the electromagnetic field. These finite-difference equations were derived by Yee and are given in Ref. 6. Here we write down the equations only for the E_z and the H_z components:

$$E_z^{n+1}(i, j, k+\tfrac{1}{2}) = E_z^n(i, j, k+\tfrac{1}{2}) + \frac{\Delta t}{\epsilon(i, j, k+\tfrac{1}{2})} \times \left[\frac{H_y^{n+1/2}(i+\tfrac{1}{2}, j, k+\tfrac{1}{2}) - H_y^{n+1/2}(i-\tfrac{1}{2}, j, k+\tfrac{1}{2})}{\Delta x} - \frac{H_x^{n+1/2}(i, j+\tfrac{1}{2}, k+\tfrac{1}{2}) - H_x^{n+1/2}(i, j-\tfrac{1}{2}, k+\tfrac{1}{2})}{\Delta y} - (\dot{P}_z)^{n+1/2}(i, j, k+\tfrac{1}{2}) \right], \tag{21a}$$

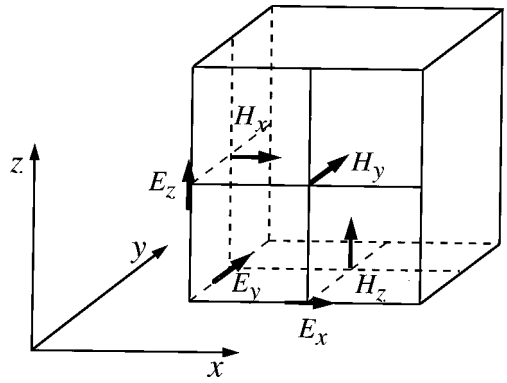

Fig. 1. Position of field components in the FDTD lattice in the 3D algorithm. The components of the dipole moment are placed in the same position as the electric-field components and are not shown.

$$H_z^{n+1/2}(i+\tfrac{1}{2}, j+\tfrac{1}{2}, k) = H_z^{n-1/2}(i+\tfrac{1}{2}, j+\tfrac{1}{2}, k) + \frac{\Delta t}{\mu_0}\left[\frac{E_x^n(i+\tfrac{1}{2}, j+1, k) - E_x^n(i+\tfrac{1}{2}, j, k)}{\Delta y} - \frac{E_y^n(i+1, j+\tfrac{1}{2}, k) - E_y^n(i, j+\tfrac{1}{2}, k)}{\Delta x} \right]. \tag{21b}$$

We assumed the dipole source has a spatial distribution of a δ function in the previous theoretical analysis. In the numerical calculation, however, such an idealization is difficult to realize, and we use the approximation that the dipole source is distributed uniformly in a unit cube. For example, for a z-polarized dipole source located at grid point $(i, j, k+\frac{1}{2})$, only $P_z(i, j, k+\frac{1}{2})$ is nonzero; all P_x, P_y, and other P_z are zero.

One problem of calculating the radiation field of a dipole in a microcavity is that we have to compute the electromagnetic field in an unbounded spatial domain. However, the computer memory is limited, and we must use some boundary condition to terminate the computational domain. In this paper we use the PML[7] boundary condition, which has the unique property of absorbing electromagnetic waves incident at any angle without reflection. The PML can be viewed as a lossy uniaxial medium,[12] characterized by parameters $(\sigma_x, \sigma_y, \sigma_z)$. Some important properties of the PML medium are summarized here. For a complete discussion of the PML and the finite-difference equations for the PML medium, readers should consult Ref. 12.

In the PML region the Maxwell equations at a given frequency ω become[12]

$$\nabla \times \mathbf{H} = i\omega\epsilon\tilde{\epsilon}\mathbf{E}, \tag{22a}$$

$$\nabla \times \mathbf{E} = -i\omega\mu_0\tilde{\mu}\mathbf{H}, \tag{22b}$$

where

$$\tilde{\epsilon} = \tilde{\mu} = \begin{bmatrix} s_y s_z/s_x & 0 & 0 \\ 0 & s_x s_z/s_y & 0 \\ 0 & 0 & s_x s_y/s_z \end{bmatrix}, \tag{23a}$$

$$s_x = 1 + \frac{\sigma_x}{j\omega\epsilon_0},$$

$$s_y = 1 + \frac{\sigma_y}{j\omega\epsilon_0},$$

$$s_z = 1 + \frac{\sigma_z}{j\omega\epsilon_0}. \tag{23b}$$

Note that if we set $(\sigma_x, \sigma_y, \sigma_z)$ to (0, 0, 0) in the above equations, $\tilde{\epsilon}$ and $\tilde{\mu}$ are equal to a unit matrix and Eq. (22) is reduced to ordinary Maxwell's equations. Therefore the usual dielectric medium can be regarded as a special case of the PML with $(\sigma_x, \sigma_y, \sigma_z)$ equal to (0, 0, 0). Next we can introduce the FDTD lattice cells shown in Fig. 1, discretize Eq. (22) on that lattice, and obtain the equations that govern the temporal evolution of the electromagnetic field in PML media. These equations are given in Ref. 12.

Theoretically, if inside the PML medium, σ_x varies only along the x direction while remaining the same along the y and the z directions, and σ_y, σ_z behave similarly, the electromagnetic wave that propagates inside the PML will be absorbed without any reflection. When this is the case, we can build the computational domain as in Ref. 13. The radiation dipole and the microcavity are placed at the center of the mesh, with the PML region surrounding them and absorbing all the outgoing electromagnetic radiation. The whole computational domain is terminated by perfect metal outside the PML. In this computational mesh the electromagnetic wave will encounter no reflection at any interface except at the outermost boundary of the perfect metal. However, we can choose PML parameters such that most of the electromagnetic waves are absorbed by the PML and the electromagnetic field at the outside boundary is negligible.

Even though the PML does not reflect any incident electromagnetic wave theoretically, Berenger[7] pointed out that if σ_x, σ_y, and σ_z are constant within the PML region in the above computational domain, significant reflection will occur because of the discrete approximation at the interface between the interior region and the PML region. So following Ref. 12, σ can be varied along the normal axis of the PML to minimize the numerical reflection. For example, along the z direction in the PML we can choose the following form for σ_z:

$$\sigma_z(z) = \frac{\sigma_{\max}|z - z_0|^m}{d^m}, \tag{24}$$

where z_0 is the coordinate of the interface of the PML and d is the total depth of the PML. σ_x and σ_y can also be chosen to have similar spatial dependence and the same $\sigma_{\max}$ along the x and the y axes, respectively. In this paper we denote this kind of PML boundary as PML $(\sigma_{\max}, d, m)$.

B. Finite-Difference Time-Domain Algorithm for the Rotationally Symmetric Geometries

The above 3D algorithm places stringent requirements on computational memory and time. The computer memory required for these 3D calculations is proportional to N^3, where N is the cell number in each direction. However, in rotationally symmetric geometries, the symmetry itself allows us to effectively reduce the original problem into one of two dimensions. Thus in this cylindrical algorithm the required memory is proportional to N^2, where N is the cell number in the r and z directions, with significant savings in computational memory and time.

Recently, Chen *et al.*[8] developed an efficient algorithm for solving Maxwell's equations in structures with rotational symmetry, which can be easily generalized to include a dipole radiation term. First, we use the rotational symmetry and assume that the electric field **E**, the magnetic field **H**, and the dipole moment **P** have the following forms in cylindrical coordinates:

$$\mathbf{E}(r, z, \phi) = \exp(im\phi)[E_r(r, z)\hat{e}_r + iE_\phi(r, z)\hat{e}_\phi + E_z(r, z)\hat{e}_z], \tag{25a}$$

$$\mathbf{P}(r, z, \phi) = \exp(im\phi)[P_r(r, z)\hat{e}_r + iP_\phi(r, z)\hat{e}_\phi + P_z(r, z)\hat{e}_z], \tag{25b}$$

$$\mathbf{H}(r, z, \phi) = \exp(im\phi)[iH_r(r, z)\hat{e}_r + H_\phi(r, z)\hat{e}_\phi + iH_z(r, z)\hat{e}_z], \tag{25c}$$

where m is an integer. In this paper we call the electromagnetic field with the above angular dependence an mth-order mode and the dipole moment with this distribution an mth-order dipole source. From the rotational symmetry we know that an mth-order dipole source can excite only the mth-order electromagnetic modes. Therefore a dipole located at the symmetry axis and polarized in the z direction is a zeroth-order dipole source, because the dipole distributes symmetrically with respect to the rotation axis, and we need to consider only the zeroth-order modes when calculating the electromagnetic field radiated by this dipole. However, for a dipole located at the center and polarized in the radial direction, we choose $m = 1$ or $m = -1$, since the dipole moment distribution depends on ϕ as a function of $\cos\phi$ and $\sin\phi$, which is a linear combination of $\exp(i\phi)$ and $\exp(-i\phi)$.

Substituting Eq. (25) into Maxwell's equations in cylindrical coordinates, we obtain the following differential equations:

$$\epsilon\frac{\partial E_r}{\partial t} = -\frac{\partial H_\phi}{\partial z} - \frac{m}{r}H_z - \frac{\partial P_r}{\partial t}, \tag{26a}$$

$$\epsilon\frac{\partial E_\phi}{\partial t} = \frac{\partial H_r}{\partial z} - \frac{\partial H_z}{\partial r} - \frac{\partial P_\phi}{\partial t}, \tag{26b}$$

$$\epsilon \frac{\partial E_z}{\partial t} = \frac{m}{r} H_r + \frac{1}{r} \frac{\partial (r H_\phi)}{\partial r} - \frac{\partial P_z}{\partial t}, \tag{26c}$$

$$-\mu_0 \frac{\partial H_r}{\partial t} = -\frac{\partial E_\phi}{\partial z} + \frac{m}{r} E_z, \tag{26d}$$

$$-\mu_0 \frac{\partial H_\phi}{\partial t} = \frac{\partial E_r}{\partial z} - \frac{\partial E_z}{\partial r}, \tag{26e}$$

$$-\mu_0 \frac{\partial H_z}{\partial t} = -\frac{m}{r} E_r + \frac{1}{r} \frac{\partial (r E_\phi)}{\partial r}. \tag{26f}$$

Following Chen,[8] we place the electromagnetic field and the dipole source in a 2D FDTD grid, as in Fig. 2, and once again evaluate the **E** and the **H** fields at alternate half-time steps. The above differential equations can then be transformed into finite-difference equations.[8] For the E_z and the H_z components, the corresponding finite-difference equations read as

$$E_z^{n+1}(i, j+\tfrac{1}{2}) = E_z^n(i, j+\tfrac{1}{2}) + \frac{\Delta t}{\epsilon(i, j+\tfrac{1}{2})} \times \left[\frac{m H_r^{n+1/2}(i, j+\tfrac{1}{2})}{r_i} + \frac{r_{i+1/2} H_\phi^{n+1/2}(i+\tfrac{1}{2}, j+\tfrac{1}{2}) - r_{i-1/2} H_\phi^{n+1/2}(i-\tfrac{1}{2}, j+\tfrac{1}{2})}{r_i \Delta r} - (\dot{P}_z)^{n+1/2}(i, j+\tfrac{1}{2}) \right], \tag{27a}$$

$$H_z^{n+1/2}(i+\tfrac{1}{2}, j) = H_z^{n-1/2}(i+\tfrac{1}{2}, j) + \frac{\Delta t}{\mu_0} \left[\frac{m E_r^n(i+\tfrac{1}{2}, j)}{r_{i+1/2}} - \frac{r_{i+1} E_\phi^n(i+1, j) - r_i E_\phi^n(i, j)}{r_{i+1/2} \Delta r} \right], \tag{27b}$$

where $r_i = (i - 1/2)\Delta r$ and $r_{1/2} = r_0 = 0$. The equations for E_r and E_ϕ, H_r and H_ϕ can be derived similarly.

Before using the above finite-difference equations to evolve the electromagnetic field, we still need the time-update equations for the electromagnetic field at the boundaries of the computational domain. Denote the FDTD lattice as (i, j), and assume the computational domain in the region of $0 \leqslant i \leqslant i_0$, $0 \leqslant j \leqslant j_0$; then the mesh boundaries consist of the cylindrical axis at $i = 0$, the two axial planes at $j = 0$ and $j = j_0$, and the outside radial boundary at $i = i_0$. At the cylindrical axis we define the FDTD lattice cells as in Ref. 8 (see Fig. 2), which are only half the size of the normal FDTD lattice cells and contain only three field components, E_r, H_ϕ, and H_z. However, among the three field components, only H_z is needed to update the adjacent fields. The time-update equation for H_z can be obtained from the path integral of the Maxwell equations. The result is given in Ref. 8:

$$H_z^{n+1/2}(0, j) = H_z^{n-1/2}(0, j) - \frac{4\Delta t}{\mu_0 \Delta r} E_\phi^n(1, j). \tag{28}$$

Since the cylindrical algorithm is much more memory efficient, in the numerical simulation we can interpose a greater volume of space between the microcavity and the absorbing boundary and effectively reduce the incident angle of the electromagnetic wave incident on the boundary. In this case we can use a boundary condition similar to Mur's absorbing boundary,[14,15] even though it is not as efficient as the PML for an electromagnetic wave with a large incident angle. But before we discuss the construction of the absorbing boundary condition in detail, we need to find out which field components we need to know at the boundary. For the axial boundary at $j = 0$ we notice that all the field components, except the two tangential electric fields E_r and E_ϕ, can be updated with the finite-difference equations derived above. However, to evaluate E_r or E_ϕ, we need to know the magnetic field outside the mesh; thus we must find the radiation boundary condition for these two tangential electric-field components. The same holds true for the boundary at $j = j_0$. For the radial boundary at $i = i_0$, the two tangential components are E_z and E_ϕ. In the following analysis we explicitly give the radiation boundary condition only for E_ϕ, since the boundary condition for E_r or E_z can be derived in a similar way.

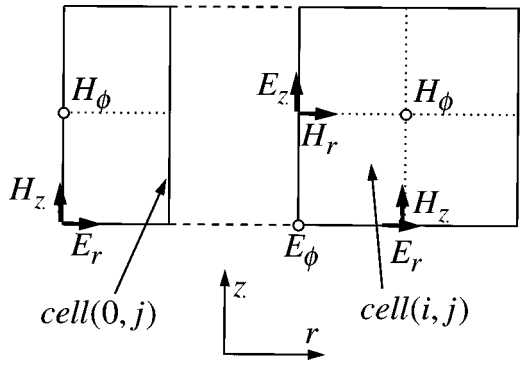

Fig. 2. Position of field components in the FDTD lattice in the cylindrical algorithm. The components of the dipole moment are placed in the same position as the electric-field components and are not shown.

To construct the absorbing boundary condition in the radial direction, we first observe that in cylindrical coordinates the radial solution of Maxwell's equations is a Bessel function of order m. So the outgoing wave has the following asymptotic form when r is large:

$$\psi(t, r, z, \phi) \to \sqrt{\frac{2}{\pi x}} \exp\left[i \left(\omega t - x + \frac{\nu \pi}{2} + \frac{\pi}{4} \right) \right] \times \exp(\pm i k_z z) \exp(i m \phi), \tag{29}$$

where $x = (\omega^2/c^2 - k_z^2)^{1/2} r = k_e r$ and c is the speed of light in dielectric material. Thus we can construct a differential equation that the outgoing wave must satisfy:

$$\frac{k_e}{\omega}\frac{\partial \psi}{\partial t} + \frac{\partial \psi}{\partial r} + \frac{1}{2r}\psi = 0. \tag{30}$$

Assuming k_z is small and expanding k_e/ω, then substituting $k_z^2 = -(\partial^2/\partial z^2)$, $\omega^2 = -(\partial^2/\partial t^2)$ into the above equation, we get

$$\left(\frac{1}{c^2}\frac{\partial^2}{\partial t^2} + \frac{1}{c}\frac{\partial^2}{\partial r\,\partial t} + \frac{1}{2cr}\frac{\partial}{\partial t} - \frac{1}{2}\frac{\partial^2}{\partial z^2}\right)\psi = 0. \tag{31}$$

From this equation, which E_ϕ and E_z should obey, we can use a finite-difference approximation and get the radial absorbing boundary condition. At the radial boundary $i = i_0$ the E_ϕ component must satisfy

$$\begin{aligned}
E_\phi^{n+1}(i_0, j) = & -\frac{1}{1 + \dfrac{c\Delta t}{4r_{i_0-1/2}} + \dfrac{c\Delta t}{\Delta r}}\Bigg[E_\phi^{n+1}(i_0 - 1, j) \\
& \times \left(1 + \frac{c\Delta t}{4r_{i_0-1/2}} - \frac{c\Delta t}{\Delta r}\right) + E_\phi^{n-1}(i_0, j) \\
& \times \left(1 - \frac{c\Delta t}{4r_{i_0-1/2}} - \frac{c\Delta t}{\Delta r}\right) + E_\phi^{n-1}(i_0 - 1, j) \\
& \times \left(1 - \frac{c\Delta t}{4r_{i_0-1/2}} + \frac{c\Delta t}{\Delta r}\right) \\
& + \left(-2 + \frac{c^2\Delta t^2}{\Delta z^2}\right)\{E_\phi^n(i_0, j) + E_\phi^n(i_0 - 1, j)\} \\
& - \frac{c^2\Delta t^2}{2\Delta z^2}\{E_\phi^n(i_0, j + 1) + E_\phi^n(i_0, j - 1) \\
& + E_\phi^n(i_0 - 1, j + 1) + E_\phi^n(i_0 - 1, j - 1)\}\Bigg].
\end{aligned} \tag{32}$$

To derive the absorbing boundary conditions in the axial direction, we first notice the following differential equation at plane $j = 0$ in Ref. 14:

$$\left[\frac{1}{c}\frac{\partial^2}{\partial z\,\partial t} - \frac{1}{c^2}\frac{\partial^2}{\partial t^2} + \frac{1}{2}\left(\frac{\partial^2}{\partial x^2} + \frac{\partial^2}{\partial y^2}\right)\right]\psi = 0. \tag{33}$$

The above result is in the rectangular Cartesian coordinates and for a computational mesh located in the region $j \geqslant 0$. However, in cylindrical coordinates,

$$\nabla_{\text{transv}}^2 = \frac{\partial^2}{\partial x^2} + \frac{\partial^2}{\partial y^2} = \frac{1}{r}\frac{\partial}{\partial r}\left(r\frac{\partial}{\partial r}\right) + \frac{1}{r^2}\frac{\partial^2}{\partial \phi^2}. \tag{34}$$

Thus for the mth-order electromagnetic field the absorbing boundary condition for E_ϕ and E_r at plane $j = 0$ becomes

$$\left[\frac{1}{c}\frac{\partial^2}{\partial z\,\partial t} - \frac{1}{c^2}\frac{\partial^2}{\partial t^2} + \frac{1}{2}\left(\frac{1}{r}\frac{\partial}{\partial r} + \frac{\partial^2}{\partial r^2} - \frac{m^2}{r^2}\right)\right]\psi = 0. \tag{35}$$

Applying the finite difference approximation to the above equation and casting the result in a form suitable for numerical computation, for E_ϕ at $j = 0$ we have

$$\begin{aligned}
E_\phi^{n+1}(i, 0) = & \frac{c\Delta t - \Delta z}{c\Delta t + \Delta z}[E_\phi^{n+1}(i, 1) + E_\phi^{n-1}(i, 0)] - E_\phi^{n-1}(i, 1) \\
& + \frac{\Delta z(2\Delta r^2 - c^2\Delta t^2)}{\Delta r^2(\Delta z + c\Delta t)}[E_\phi^n(i, 0) + E_\phi^n(i, 1)] \\
& - \frac{m^2}{2r_i^2}\frac{c^2\Delta t^2\Delta z}{c\Delta t + \Delta z}[E_\phi^n(i, 0) + E_\phi^n(i, 1)] \\
& + \frac{c^2\Delta t^2\Delta z}{c\Delta t + \Delta z}\frac{1}{2\Delta r}\left(\frac{1}{\Delta r} + \frac{1}{2r_i}\right) \\
& \times [E_\phi^n(i + 1, 0) + E_\phi^n(i + 1, 1)] \\
& + \frac{c^2\Delta t^2\Delta z}{c\Delta t + \Delta z}\frac{1}{2\Delta r}\left(\frac{1}{\Delta r} - \frac{1}{2r_i}\right) \\
& \times [E_\phi^n(i - 1, 0) + E_\phi^n(i - 1, 1)].
\end{aligned} \tag{36}$$

4. NUMERICAL RESULTS

In this section we use the above two algorithms to calculate the modification of the spontaneous emission rate in three different geometries. The first example is a waveguide formed by two parallel perfect metal plates. In this case an analytical formula for the spontaneous emission rate was given in Ref. 5 and is used to test the validity of our method by comparison of the numerical results with the analytical results. The second problem involves the spontaneous emission rate of an atom in a dielectric slab waveguide. The waveguide modes are shown to have a strong influence on the spontaneous emission rate. Finally, a dielectric microdisk is studied to show the usefulness of our algorithm. The microdisk cavity is of practical interest, because it is possible to achieve a large spontaneous emission factor in such a structure.[16] To calculate the spontaneous emission factor, we need to know the spontaneous emission rate in such a structure. However, the microdisk structure is more complicated, and an analytical calculation of the spontaneous emission lifetime is difficult. But it can be readily obtained with our algorithm. In this last example we compute the spontaneous emission rate in a dielectric microdisk as a function of the dipole emission frequency.

In all the calculations the units are normalized such that ϵ_0 and μ_0 equal 1 (therefore $c = 1$). Also, we normalize $\Delta x = \Delta y = \Delta z = 1$ in the 3D calculation, and $\Delta r = \Delta z = 1$ in the cylindrical calculation.

A. Dipole between Two Parallel Perfect-Metal Plates

In this example we place a dipole at the center of the two parallel metal plates and calculate the spontaneous emission rate as the function of the spacing between the metal plates. Two dipole polarizations are considered: dipole normal to the metal plates (axial dipole) and dipole par-

allel to the metal plates (radial dipole). The results for the radial dipole and the axial dipole are shown in Figs. 3 and 4, respectively.

The theoretical value for the spontaneous emission rate is obtained with an infinite set of image dipoles[5] and is given in Figs. 3 and 4 as solid curves. Many interesting features of the theoretical result can also be readily explained by the TE and the TM modes of the parallel-mirror waveguide.[5] For example, the spontaneous emission rate of the radial dipole (see Fig. 3) increases suddenly when the metal plate spacing L reaches $\lambda/2$, $3\lambda/2$,..., which are the cutoff thicknesses for the $TE_0, TE_2, \ldots$ modes in a parallel-mirror waveguide. Also notice that in Fig. 3 the spontaneous emission rate is 0 when $L < 0.5\lambda$. This is because only the TM_0 mode exists in this metal waveguide when $L < 0.5\lambda$, and according to Eq. (15) the radial dipole does not couple to the TM_0 mode and therefore cannot radiate any power. For the axial dipole that couples only to TM modes the spontaneous emission rate depends less on the waveguide modes. But we can still identify the change of spontaneous emission rate at $L/\lambda = 1, 2, \ldots$ as caused by the appearance of the $TM_2, TM_4, \ldots$ modes. It is also clear from our theoretical results that the waveguide modes with odd symmetry in the axial direction, such as the TE_1, $TM_1, TE_3, TM_3, \ldots$ modes, have no influence on the dipole spontaneous emission rate. The reason is that such modes have a node at the center of the waveguide. Therefore the dipole does not couple to such modes.

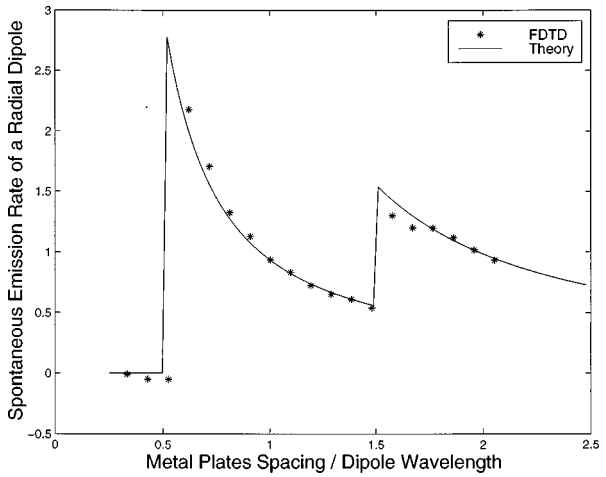

Fig. 3. Spontaneous emission rate of a radial dipole between two metal plates. The dipole is polarized parallel to the metal plates and placed at the center of the two metal plates. The spontaneous emission rate is normalized to the corresponding free-space value.

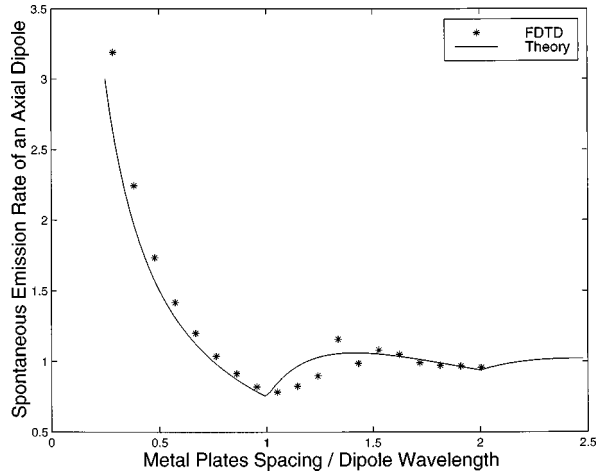

Fig. 4. Spontaneous emission rate of an axial dipole between two metal plates. The dipole is polarized normal to the metal plates and placed at the center of the two metal plates. The spontaneous emission rate is normalized to the corresponding free-space value.

For the numerical calculation of the spontaneous emission rate we use the cylindrical algorithm. The dipole frequency is 0.3 in normalized units, corresponding to a vacuum wavelength of 20.94 cells. The radius of the metal plates is 80 cells. Comparing the theoretical results with the numerical results, we can see that the agreement between theory and computation is good. The deviation between the calculated values and the theoretical values is likely due to two effects. When the dipole is close to the metal plates, the difference is due to the finite size of the dipole. (In theoretical calculations, we use a δ function for the dipole distribution. However, in our FDTD calculations the dipole occupies a unit cell.) Second, when the dipole is relatively far from the metal plates, the difference is caused by the finite reflectivity at the absorbing boundary. By changing the width of the waveguide, we effectively change the angular distribution of the electromagnetic modes, which causes the reflectivity at the absorbing boundary to vary, as discussed above, and results in the deviation from theoretical analysis.

In Fig. 3, when the metal plate spacing is less than $\lambda/2$, the cutoff value for the TE modes, the numerical simulation gives some small negative values for the spontaneous emission rate, which we believe is caused by the numerical error that is due to the longitudinal electromagnetic field. We recall that the electromagnetic field given by our algorithm satisfies all four of Maxwell's equations, as explained in Appendix B, and thus contains both the transverse component and the longitudinal one. In the case of radial polarization and $L < \lambda/2$, the dipole can no longer excite the transverse modes and the electromagnetic field consists only of the longitudinal part, which can be quite large near the dipole source. Therefore, even though the theoretical radiation power should be 0, the numerical error from the large longitudinal electromagnetic field will give a small nonzero value for the spontaneous emission rate.

B. Dipole in a Dielectric Slab Waveguide

Here we calculate the spontaneous emission lifetime of a dipole at the center of a semiconductor ($n = 3.6$) slab waveguide. The dipole frequency is 0.08, which corresponds to a wavelength of 21.8 cells in semiconductor and 78.5 cells in air. As in the previous calculation, we compute the spontaneous emission rate for two dipole polarizations: axial polarization and radial polarization. The spontaneous emission rate is then normalized to the free-space emission rate. For the absorbing boundaries, we use PML(12.0, 8, 4). The result is shown in Fig. 5.

The electromagnetic modes of a dielectric waveguide have been analyzed extensively in the literature.[17] These modes can be classified into two types: radiation

modes and waveguide modes. The waveguide modes can be further classified into TE and TM modes, according to the different polarizations of these modes. The general features of TE and TM modes are quite similar, except that the nth-order TE mode is more strongly confined than the TM mode of the same order. For a symmetric waveguide the waveguide thickness D has the same cutoff value for TE and TM modes[17]:

$$\frac{D_{\text{cutoff}}}{\lambda} = \frac{n_2}{2(n_2^2 - n_1^2)^{1/2}} m, \tag{37}$$

where m is an integer and refers to the mth TE or TM mode, D_{cutoff} is the cutoff thickness for that particular mode, λ is the wavelength in the dielectric waveguide, n_2 is the waveguide refractive index, and n_1 is the refractive index of the surrounding medium. In our calculation, $n_2 = 3.6$ and $n_1 = 1$. With these parameters, the cutoff value of D/λ for the mth TE and TM mode is

$$\frac{D_{\text{cutoff}}}{\lambda} = 0.52m, \qquad m = 0, 1, 2, \ldots . \tag{38}$$

From Eq. (15) we can see that the coupling strength of the dipole to a particular mode is proportional to the electric field of that mode at the dipole position and therefore inversely proportional to the effective mode volume for that mode. Since TE modes are more tightly confined, the effective mode volume is smaller, which results in a larger coupling between the dipole and the TE modes. Also from Eq. (15), it is clear that the radial dipole couples strongly to the TE modes and weakly to the TM modes; however, the axial dipole couples to TM modes only. Thus we can expect that the coupling between the waveguide modes and the radial dipole will be stronger than the coupling in the axial dipole case. As a consequence the spontaneous emission rate of the radial dipole will be more sensitive on the waveguide thickness than the axial dipole. The numerical results in Fig. 5 clearly show that the spontaneous emission rate of the radial dipole depends more strongly on the waveguide thickness, in agreement with our theoretical expectation.

As in the previous example there is no coupling between the radial dipole and the odd TE modes, because of the odd symmetry of their product. Thus we expect an increase of the spontaneous emission rate when the cutoff thickness for the TE_2, TE_4, ... modes is reached, but the appearance of the TE_1, TE_3, ... modes should not significantly change the radial dipole spontaneous emission rate, as seen in Fig. 5.

C. Dipole in a Dielectric Microdisk

For the calculation of spontaneous emission rate in a dielectric microdisk we take the cavity refractive index as $n = 3.4$. As in the previous two examples we consider two dipole polarizations: a radial dipole and an axial dipole. For the absorbing boundaries we use PML(12.0, 8, 4).

In the case of a radial dipole we use a microdisk with a thickness of 12 cells in the z direction and a radius of 42 cells in the xy plane. The dipole is polarized in the x direction. The displacement between the dipole and the origin of the microdisk is 32 cells in the x direction, and the dipole is located at the center of the cavity in the y and the z directions. The dielectric structure is fixed, and the dipole frequency is changed from 0.0439 to 0.0610, which is equivalent to changing the vacuum wavelength from 143.13 cells to 103.00 cells. The results are shown in Fig. 6. The unit of the horizontal axis is D/λ, where D is the microdisk thickness and λ is the dipole emission wavelength in semiconductor. In this figure we also show the spontaneous emission rate of a radial dipole at the center of a dielectric slab waveguide with a thickness of 12 cells and $n = 3.4$.

In Fig. 6 the spontaneous emission rate of a radial dipole in a slab waveguide is almost a constant in the frequency range of interest to us. However, the result of the microdisk differs drastically from that of the slab waveguide, which clearly shows a peak near $D/\lambda = 0.38$, corresponding to the dipole emission frequency of 0.0585. This peak could be due to the appearance of high-Q whispering gallery modes.[16] Also notice that in our result

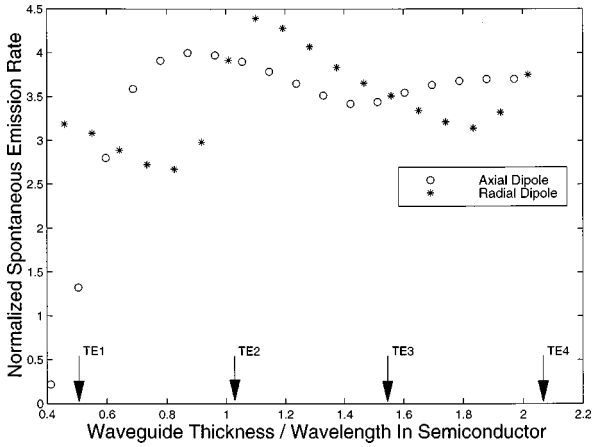

Fig. 5. Spontaneous emission rate of axial and radial dipoles in a semiconductor waveguide. The dipole is placed at the center of the semiconductor waveguide. The spontaneous emission rate is normalized to the corresponding free-space value. The arrows indicate the cutoff thickness of the TE modes.

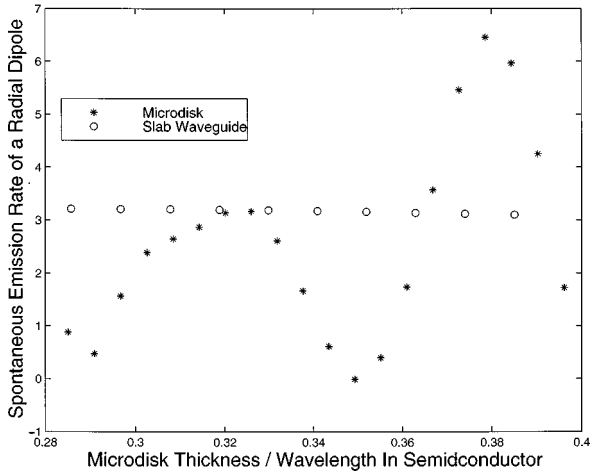

Fig. 6. Spontaneous emission rate of a radial dipole in a semiconductor microdisk (star), spontaneous emission rate of a radial dipole in a slab waveguide (circle). The dipole polarizes in the x direction. The spontaneous emission rate is normalized to the corresponding free-space value.

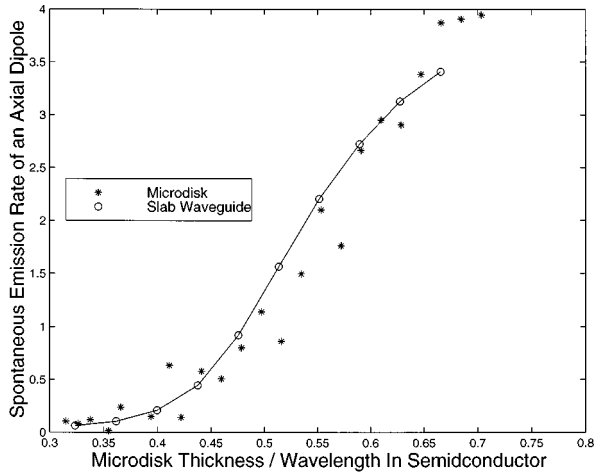

Fig. 7. Spontaneous emission rate of an axial dipole in a semiconductor microdisk (star), spontaneous emission rate of an axial dipole in a slab waveguide (circle). We connected the circles with a solid curve to make them more obvious. The dipole polarizes in the z direction. The spontaneous emission rate is normalized to the corresponding free-space value.

there is one point, $D/\lambda \approx 0.35$, that gives a small negative spontaneous emission rate, which is simply a numerical artifact, as explained in Subsection 4.A.

For an axial dipole we change the thickness of the microdisk to 13 cells in the z direction. The dipole is now polarized in the z direction. All other parameters remain the same. The dipole frequency is varied between 0.0448 and 0.100, corresponding to a change in vacuum wavelength between 140.25 and 62.83 cells. The result for the spontaneous emission rate is shown in Fig. 7, along with the spontaneous emission rate of an axial dipole at the center of an infinite slab waveguide with the same thickness, 13 cells and $n = 3.4$.

It is clear from Fig. 7 that for the axial dipole the spontaneous emission rate in a microdisk is essentially the same as the spontaneous emission rate in a slab waveguide, which is quite different from what we have seen in the radial dipole case. This result also indicates that the peak in Fig. 6 is consistent with a whispering gallery mode, since such a mode cannot couple to an axial dipole.[16] Furthermore, in Fig. 7 the spontaneous emission rates for an axial dipole in the microdisk fluctuate near the corresponding values for an equivalently sized slab waveguide, which probably suggests some weak coupling between the axial dipole and other resonant modes in the microdisk.

5. SUMMARY

In summary, we have developed two FDTD algorithms to calculate the spontaneous emission lifetime in microcavities. We have calculated the spontaneous emission lifetime in a metal waveguide and see good agreement between FDTD calculations and theoretical results. We have also calculated the spontaneous emission lifetime in a dielectric slab waveguide. Our result shows the strong influence of the TE modes on the spontaneous lifetime of a radial dipole. In the case of a microdisk we observe a peak in the spontaneous emission rate for the radial dipole, which is probably due to the whispering gallery modes in the microdisk.

APPENDIX A

It is mentioned above that only the transverse electric field contributes to the radiation power. Here we prove this assertion.

Start from the inhomogeneous Maxwell equations

$$\nabla \cdot \mathbf{D} = \rho, \tag{A1a}$$

$$\nabla \times \mathbf{E} = -\frac{\partial \mathbf{B}}{\partial t}, \tag{A1b}$$

$$\nabla \cdot \mathbf{B} = 0, \tag{A1c}$$

$$\nabla \times \mathbf{H} = \frac{\partial \mathbf{D}}{\partial t} + \mathbf{J} \tag{A1d}$$

and express the field in terms of a scalar potential Φ and a vector potential $\mathbf{A}$:

$$\mathbf{B} = \nabla \times \mathbf{A}, \tag{A2a}$$

$$\mathbf{E} = -\nabla\Phi - \frac{\partial \mathbf{A}}{\partial t}. \tag{A2b}$$

In this paper we have a nonuniform distribution of dielectric constant; correspondingly, the transverse condition for a vector field $\mathbf{F}(\mathbf{x})$ should be generalized as[11]

$$\nabla \cdot [\epsilon(\mathbf{x})\mathbf{F}] = 0. \tag{A3}$$

Now, when we require that the vector potential satisfy the above transverse condition, which is a natural generalization of the Coulomb gauge, the Maxwell equations are reduced to

$$\nabla \cdot [\epsilon(\mathbf{x})\nabla\Phi] = -\rho, \tag{A4a}$$

$$\nabla \times [\nabla \times \mathbf{A}] + \epsilon\mu_0 \frac{\partial^2 \mathbf{A}}{\partial t^2} = \mu_0 \mathbf{J}_{\text{tran}} = \mu_0 \left[\mathbf{J} - \epsilon \frac{\partial}{\partial t} \nabla\Phi\right]. \tag{A4b}$$

The right-hand term of the above equation represents a transverse current density, which can be easily verified when we take the divergence and impose the current continuity condition.

Since we consider only harmonic current source in this paper, the power radiated by such current source is given by

$$\overline{\int d^3x \mathbf{J} \cdot \mathbf{E}} = \overline{\int d^3x \mathbf{J} \cdot \mathbf{E}_{\text{long}}} + \overline{\int d^3x \mathbf{J} \cdot \mathbf{E}_{\text{tran}}} = \overline{\int d^3x \mathbf{J} \cdot [-\nabla\Phi]} + \overline{\int d^3x \mathbf{J} \cdot \left[-\frac{\partial \mathbf{A}}{\partial t}\right]}, \tag{A5}$$

where the long overbar indicates time average and we have defined the longitudinal electric field as $\mathbf{E}_{\text{long}} = -\nabla\Phi$ and the transverse electric field as $\mathbf{E}_{\text{tran}} = -\partial\mathbf{A}/\partial t$. Then using partial integration and current

continuity condition, we rewrite the term that represents the contribution from the longitudinal field as

$$\overline{\int d^3x \mathbf{J} \cdot \nabla\Phi} = \overline{\int d^3x \Phi[-\nabla \cdot \mathbf{J}]} = \overline{\int d^3x \Phi \frac{\partial \rho}{\partial t}}. \tag{A6}$$

In the case of harmonic source the $\rho(\mathbf{x}, t)$ can be separated into a time-independent part $\tilde{\rho}(\mathbf{x})$ and a periodic function in time $f(t)$. From Eq. (A4a) we realize that the scalar potential $\Phi(\mathbf{x}, t)$ can be separated also into a time-independent part $\tilde{\Phi}(\mathbf{x})$ and the same periodic function $f(t)$. Therefore the above time average is simplified as

$$\overline{\int d^3x \mathbf{J} \cdot \nabla\Phi} = \frac{1}{2}\overline{\int d^3x \frac{\partial}{\partial t}[\Phi\rho]}. \tag{A7}$$

Finally, finishing the time average, we arrive at

$$\overline{\int d^3x \mathbf{J} \cdot \mathbf{E}_{\text{long}}} = -\lim_{T\to\infty}\frac{1}{2T}\left[\left\{\int d^3x \Phi(\mathbf{x}, t)\rho(\mathbf{x}, t)\right\}_{t=T} - \left\{\int d^3x \Phi(\mathbf{x}, t)\rho(\mathbf{x}, t)\right\}_{t=0}\right]. \tag{A8}$$

Since both $\Phi(\mathbf{x}, t)$ and $\rho(\mathbf{x}, t)$ are periodic functions in time, the above equation averages to zero and therefore

$$P_{\text{classical}} = \overline{\int d^3x \mathbf{J} \cdot \mathbf{E}} = \overline{\int d^3x \mathbf{J} \cdot \mathbf{E}_{\text{tran}}}, \tag{A9}$$

which means only the transverse electric field contributes to the dipole radiation power.

APPENDIX B

In the FDTD algorithm, we use only two of Maxwell's equations to update the electromagnetic field. However, all four of them are generally needed to determine the field. Here we prove that the electromagnetic field given by FDTD calculations is indeed the solution of Maxwell's equations.

The two equations used in the FDTD algorithm are

$$\nabla \times \mathbf{E} = -\frac{\partial \mathbf{B}}{\partial t}, \tag{B1a}$$

$$\nabla \times \mathbf{H} = \frac{\partial \mathbf{D}}{\partial t} + \frac{\partial \mathbf{P}}{\partial t}. \tag{B1b}$$

Taking the divergence of both sides of Eq. (B1) and applying the following vector identity

$$\nabla \cdot [\nabla \times \mathbf{F}(\mathbf{x})] = 0, \tag{B2}$$

we obtain

$$\frac{\partial}{\partial t}\nabla \cdot \mathbf{B} = 0, \tag{B3a}$$

$$\frac{\partial}{\partial t}\nabla \cdot \mathbf{D} = -\frac{\partial}{\partial t}\nabla \cdot \mathbf{P}. \tag{B3b}$$

If at the beginning of the simulation we set both the field and the dipole distribution to zero, integrating the above equations with respect to time leads to

$$\nabla \cdot \mathbf{D} = -\nabla \cdot \mathbf{P}, \tag{B4a}$$

$$\nabla \cdot \mathbf{B} = 0. \tag{B4b}$$

Combined with Eq. (B1), they are the four Maxwell equations with a charge density of $-\nabla \cdot \mathbf{P}$ and a current density of $\partial\mathbf{P}/\partial t$.

ACKNOWLEDGMENTS

This research was sponsored by the U.S. Army Research Office, the U.S. Office of Naval Research, and the National Science Foundation. R. K. Lee and O. J. Painter also acknowledge support from the National Science and Engineering Research Council of Canada.

Y. Xu's e-mail address is yong@cco.caltech.edu.

REFERENCES

1. E. M. Purcell, "Spontaneous emission probabilities at radio frequencies," Phys. Rev. **69**, 681 (1946).
2. T. Baba, "Photonic crystals and microdisk cavities based on GaInAsP-InP system," IEEE J. Sel. Topics Quantum Electron. **3**, 808–830 (1997).
3. E. Yablonovitch, "Inhibited spontaneous emission in solid-state physics and electronics," Phys. Rev. Lett. **58**, 2059–2062 (1987).
4. J. D. Joannopoulos, R. D. Meade, and J. N. Winn, *Photonic Crystals* (Princeton University, Princeton, N.J., 1995).
5. E. A. Hinds, "Perturbative cavity quantum electrodynamics," in *Cavity Quantum Electrodynamics*, P. R. Berman, ed. (Academic, New York, 1994).
6. K. S. Yee, "Numerical solution of initial boundary value problems involving Maxwell's equations in isotropic media," IEEE Trans. Antennas Propag. **14**, 302–307 (1966).
7. J. P. Berenger, "A perfectly matched layer for the absorption of electromagnetic waves," J. Comput. Phys. **114**, 185–200 (1994).
8. Y. Chen, R. Mittra, and P. Harms, "Finite-difference time-domain algorithm for solving Maxwell's equations in rotationally symmetric geometries," IEEE Trans. Microwave Theory Tech. **44**, 832–839 (1996).
9. C. H. Henry and R. F. Kazarinov, "Quantum noise in photonics," Rev. Mod. Phys. **68**, 801–853 (1996).
10. J. D. Jackson, *Classical Electrodynamics* (Wiley, New York, 1975).
11. R. J. Glauber and M. L. Lewenstein, "Quantum optics of dielectric media," Phys. Rev. A **43**, 467–491 (1991).
12. S. D. Gedney, "An anisotropic perfectly matched layer-absorbing medium for the truncation of FDTD lattices," IEEE Trans. Antennas Propag. **44**, 1630–1639 (1996).
13. J. P. Berenger, "Three-dimensional perfectly matched layer for the absorption of electromagnetic waves," J. Comput. Phys. **127**, 363–379 (1996).
14. G. Mur, "Absorbing boundary conditions for the finite-difference approximation of the time-domain electromagnetic-field equations," IEEE Trans. Electromagn. Compat. **EMC-23**, 377–382 (1981).
15. M. Fusco, "FDTD algorithm in curvilinear coordinates," IEEE Trans. Antennas Propag. **38**, 76–89 (1990).
16. M. K. Chin, D. Y. Chu, and S. T. Ho, "Estimation of the spontaneous emission factor for microdisk lasers via the approximation of whispering gallery modes," J. Appl. Phys. **75**, 3302–3307 (1994).
17. A. Yariv and P. Yeh, *Optical Waves in Crystals* (Wiley, New York, 1984).